Oxidation Through Coating Cracks of SiC-Protected Carbon/Carbon

Nathan S. Jacobson* and Don J. Roth
National Aeronautics and Space Administration
Glenn Research Center
Cleveland, Ohio 44135
*E-mail: nathan.s.jacobson@nasa.gov

Richard W. Rauser
University of Toledo
Toledo, Ohio 43606

James D. Cawley
Case Western Reserve University
Cleveland, Ohio 44106

Donald M. Curry
National Aeronautics and Space Administration
Johnson Space Center
Houston, Texas 77058

Abstract

The oxidation of SiC-protected carbon/carbon through machined slots and naturally occurring craze cracks in the SiC was studied. The slot and crack geometries were characterized, and the subsurface oxidation of the carbon/carbon substrate at temperatures of 1000 to 1300 °C in air was assessed using weight change, x-ray computed tomography, and optical microscopy of sections. Rate constants were derived from these measurements and compared with a two-step diffusion control model of carbon oxidation. Oxidation kinetic measurements on both the specimens with machined slots and with naturally occurring craze cracks showed good agreement with the model.

Keywords: Carbon/carbon; Oxidation; Coatings; Silicon Carbide; Non-destructive Evaluation

1. Introduction

1.1 Reinforced Carbon/Carbon

Fig. 1 is a schematic of reinforced carbon/carbon (RCC) with a SiC conversion coating used on the Space Shuttle Orbiter nose cap and wing leading edges. The material is made with a two-dimensional layup of carbon-carbon fabric with repeated applications of a liquid carbon precursor to fill voids [1]. The resultant high strength and light weight make it an ideal aerospace material; however, oxidation is a major concern. An oxidation protection system is based on a SiC conversion coating. Because of the difference in coefficient of thermal expansion (CTE) of the SiC coating and carbon/carbon substrate, the SiC coating shrinks more than the underlying carbon/carbon on cooldown from the coating application temperature. This leads to vertical cracks in the coating, and these cracks are pathways for oxygen to reach the carbon/carbon substrate. Actual RCC used on the orbiters contains glass sealants to plug the cracks; however, this work examines carbon/carbon with only SiC.

The crack morphologies in a similar system have been thoroughly characterized in an elegant study by Yurgartis et al. [2]. Both surface (plan) views and section views of the material were taken to obtain information such as crack spacing, crack width, and crack morphology. Such parameters were obtained for RCC in this study and prove critical to modeling oxidation. Buchanan and Little [3] have also characterized the crack pattern in a range of SiC coatings on carbon/carbon at various deposition conditions.

1.2 Oxidation Through Coating Cracks

Figs. 2(a-b) illustrate typical oxidation voids formed due to oxygen diffusion through a coating slot or crack, respectively, and subsequent reaction. A recent study by the authors outlines the microstructural features which

1

distinguish this void from a processing void [4]. In general, an oxidation void is associated with a path for oxygen ingress (i.e., the slot in Fig. 2(a) and crack in Fig. 2(b)). At higher temperatures (>1000 °C) these oxidation processes are expected to be diffusion controlled. Diffusion control implies a lack of preferential oxidative attack and hence uniform attack of the carbon/carbon with a plane interface at the void boundary, as illustrated in Fig. 1. However, a close examination of the voids in Figs. 2(a-b) indicates some preferential attack along fiber edges and the resultant "pointed fibers," which are characteristic of reaction control [5]. Thus the actual process is a mix of diffusion and reaction control. It will be shown that diffusion control dominates.

There are numerous studies of carbon oxidation through cracks and fissures in the protective coating and associated models found in the literature. Medford [6] developed models of oxidation for RCC, assuming pathways for oxygen are the cracks and fissures in SiC. His model encompasses the following processes:

(1) Diffusion of oxygen inward through the cracks and/or fissures in the SiC
(2) Oxidation of SiC crack walls to form SiO_2
(3) Oxidation of carbon/carbon—matrix, fibers, or both
(4) Diffusion of CO outward through the cracks/fissures in the SiC

Medford developed total mass change expressions based on these processes. The expressions were the diffusion equations with modifications for the area of reaction. First he examined the case below 982 °C, where passive oxidation of the SiC is thought to be negligible; then he examined the case above 982 °C, where passive oxidation of the SiC is thought to be significant.

The general process of carbon oxidation in a nonreactive matrix or through a nonreactive coating has been explored by several investigators [7]-[13]. Carbon oxidizes to CO(g):

$$C(s) + \tfrac{1}{2} O_2(g) = CO(g) \tag{1}$$
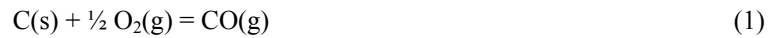
However, thermochemically the equilibrium between O_2, CO, and CO_2 favors the products in the following reaction:

$$\tfrac{1}{2}O_2(g) + CO(g) = CO_2(g) \tag{2}$$

Thus $O_2(g)$ and CO(g) cannot coexist in similar amounts—they immediately will react to form $CO_2(g)$. However, the pairs of species in reaction (2), CO(g) with $CO_2(g)$ and $O_2(g)$ with $CO_2(g)$, may coexist. Thus a two-step oxidation process is required to model carbon oxidation. The two reactions are

1. At the carbon/gas interface:

$$C(s) + CO_2(g) = 2CO(g) \tag{3}$$

Note that $CO_2(g)$ is the oxidizing species.

2. At a distance away from the carbon/gas interface:

$$CO(g) + \tfrac{1}{2}O_2(g) = CO_2(g) \tag{4}$$

In an earlier paper [13], the authors adapted this two-step diffusion-controlled oxidation model to cylindrical pinholes in the coating. Actual oxidation damage was assessed with weight loss measurements and area measurement of oxidation voids below the pinholes, using cross sections. At 1400 and 1000 °C hemispherical voids were observed on a macroscopic scale, indicating uniform attack and diffusion control. The two-step model described the process reasonably well at 1400 and 1000 °C. However, at 600 °C only minimal oxidation was measured, and reaction control dominated. Hence the model did not fit at this lower temperature.

In the present study, the two-step oxidation model is further extended to describe a half-cylinder trough which forms under a slot or craze crack in the SiC coating. First a series of experiments is performed using machined slots in the coating. This allows testing the model with well-defined oxygen pathway geometry. Then the study is extended to actual through-thickness craze cracks in the coating. Oxidation damage is assessed with cross-sectional views, interrupted or real-time weight loss measurements, and x-ray computed tomography scans. The kinetics of carbon consumption is then compared with the model.

2. Experimental

2.1 Characterization of Slots and Cracks in Test Specimens

The tests described here were done on 1.91-cm-diameter RCC disks with a SiC coating on all sides. These disks were obtained from Lockheed-Martin Missiles and Fire Control in Dallas, Texas. Two sets of experiments were completed. Specimens with machined slots were used for the first set; specimens with naturally occurring craze cracks were used for the second set. Prior to oxidation, both types of specimens were characterized in order to quantify the area of exposed carbon.

In the first set of specimens, artificial craze cracks with well-defined geometries were made with diamond blades (Keen Kut Products, Hayward, CA) of 0.25, 0.51, 0.76, and 1.02 mm thicknesses. These slots were cut to the SiC/carbon-carbon interface. These slotted specimens are shown in Fig. 3. One slot was cut in each specimen where the oxidation kinetics was followed with weight losses; however, two slots of different dimensions were cut in the specimens where the kinetics was followed using microstructure examination and/or x-ray computed tomography. Slot dimensions were carefully measured with a traveling microscope as well as directly from the cross sections and reported in the results section. Total coating thicknesses were measured from cross sections. Because of the variation in coating thickness, 20 random measurements were taken and averaged.

The second set of specimens contained only the naturally occurring craze cracks. These were characterized with techniques similar to Yurgartis et al. [2]. Examination of the surface (plan view) did not reveal the complete crack pattern; however, grinding ~300 μm of SiC clearly revealed the crack pattern, which was then traced, as illustrated in Figs. 4(a) and (b). Image analysis software (Adobe Photoshop CS2 (Adobe Systems, Inc., San Jose, CA) with Fovea Pro 4.0 (Reindeer Graphics, Asheville, NC)) was used to determine the total crack length per unit area. The view of a section, as shown in Fig. 5, allowed measurements of crack width at room temperature. Several such sections were examined, and an average of 10 measurements is reported. Crack widths were measured near the surface and the small narrowing of the cracks closer to the carbon/carbon was ignored for this approximate characterization. The approximate area of exposed carbon/carbon per unit area of sample is determined by multiplying the crack width by the crack length per unit area.

The measured values are listed in Table I and compared to the values reported by Yugartis et al. [2] and Buchanan and Little [3]. "Specimen A" of Yurgartis et al. is SiC-coated carbon/carbon with no matrix inhibitor; "Specimen B" is SiC-coated carbon/carbon with a boron-based matrix inhibitor. It should be noted that the materials examined by Yugartis et al. [2] and Buchanan and Little [3] are different from the RCC materials in this study. Here, the RCC had a thicker SiC coating applied by a pack cementation process than the other specimens in which the coating was applied by a chemical vapor deposition process. Yugartis et al. examined cracks that did and did not transverse the entire coating thickness. In this study only through-thickness cracks are examined. Differences in the specific CTE of carbon/carbon and the applied coating would be expected to have a major effect on the crack parameters. Thus the differences listed in Table I are not unexpected. It is interesting that despite the differences in crack width and spacing, the ratio of the exposed area of carbon to the surface area of the sample is roughly the same for all materials.

2.2 Oxidation Treatments and Sample Analyses

The samples were oxidized in air in either a box furnace or a vertical tube furnace. The kinetics of the box furnace exposures were followed with weight measurements every 0.5 hr for a total of 2.5 hr at 1200 °C. The craze crack specimens were suspended from a Cahn C–1000 (Cahn Instruments, Cerritos, CA) recording electrobalance by a sapphire fiber with a platinum wire basket into the vertical tube furnace. To avoid platinum silicide formation, the platinum wire was lined with alumina beads. Bottled air at 1 atm (101 325 Pa) was used at a flow rate of 1.67×10^{-3} liter/s, and isothermal oxidation tests were performed at 1000, 1100, 1200, and 1300 °C.

Selected samples were mounted and sectioned for optical microscopy to obtain measurements of oxidation void size. A specialized sample preparation procedure involved a premount of the entire sample in epoxy. A standard vacuum infiltration was done followed by a high-pressure application to fill the open porosity. Then the sample was sectioned, remounted in a standard metallographic mold, and polished with diamond pastes. This ensured clear microstructures and preserved the interface between the SiC and the carbon/carbon.

X-ray computed tomography (CT) was used to provide additional images of the oxidation damage, without sectioning. This SmartScan Model 100 (CITA Systems, Inc., Pueblo, CA) system utilizes a Feinfocus FXE–160 (COMET AG, Flamatt, Switzerland) microfocus x-ray source to produce very high-resolution imaging of samples,

approaching 25 μm, in the CT mode of operation. The major hardware components of this system included the x-ray source, an area detector system, a five-axis object positioning subassembly, and a lead-lined radiation cabinet. A dual-processor computer system controlled the data acquisition and image processing. The slice plane thickness was 120 μm per slice for these samples. Putting together slices electronically gave a three-dimensional view of oxidation damage.

3. Diffusion-Control Oxidation Model

3.1 Diffusion through Slot or Crack Alone

Fig. 6 is a schematic of the two-step diffusion-controlled model for oxidation through a slot or crack. Note that CO_2 is the oxidizer and reaction (3) occurs at position $x = 0$ whereas reaction (4) occurs at position $x = x_f$. A list of symbols used in this report is in the appendix to aid the reader. The following derivation is an adaptation of this standard two-step diffusion controlled model [7-13] to the coating slot or crack geometry.

The molar flux, J_i (in weight/unit area-unit time), of each species, i, is defined by

$$J_i = D_i^{eff}\left(\frac{\partial c_i}{\partial x}\right) + v_i^{ave} c_i \tag{5}$$

The first term is the diffusive term and the second is the convective term. Here $D_{i,\,eff}$ is the effective gas phase diffusivity, c_i is the molar concentration of species i (i = CO, CO_2, or O_2), and x is the distance down the slot or crack. The average molar velocity v_i^{ave} is defined as

$$v_i^{ave} = \frac{\sum_i c_i v_i}{\sum_i c_i} = \frac{\sum_i J_i}{c_T} \tag{6}$$

Here c_T is the sum of concentrations. Equation (5) becomes

$$J_i = D_i^{eff}\left(\frac{\partial c_i}{\partial x}\right) + \frac{c_i}{c_T}\sum_i J_i \tag{7}$$

The boundary conditions are shown in Fig. 6(b):

$$\text{At } x = 0: \quad c_{CO} = c_{CO}^0 \quad c_{CO_2} = c_{CO_2}^0$$

$$\text{At } x = x_f: \quad c_{CO_2} = c_{CO_2}^* \quad c_{O_2} = c_{CO} = 0 \tag{8}$$

$$\text{At } x = L: \quad c_{O_2} = c_{O_2}^L \quad c_{CO_2} = 0$$

As shown in Fig. 6(b) L is the total crack depth, which is the coating thickness.

Consider the fluxes in Region 1 (Fig. 6(a)). Here $J_{O_2}^I = -J_{CO_2}^I$ and hence the convective term in equation (7) is zero. The fluxes of $O_2(g)$ and $CO_2(g)$ in this region are thus calculated as

$$J_{O_2}^I = -D_{O_2}\left(\frac{\partial c_{O_2}}{\partial x}\right) = \frac{-D_{O_2} c_{O_2}^L}{(L - x_f)} \tag{9a}$$

4

$$J^{I}_{CO_2} = D_{CO_2}\left(\frac{\partial c_{CO_2}}{\partial x}\right) = \frac{D_{CO_2}\, c^{*}_{CO_2}}{\left(L - x_f\right)} \tag{9b}$$

A determination of the CO_2 flux emerging from the crack or slot, $J^{I}_{CO_2}$, is the ultimate goal, because it is a measure of carbon consumption. First the quantity x_f is needed. This can only be obtained as the ratio x_f/L, which is derived from the following equations (eqs. (10) to (17)). The two fluxes in equation (9) are equal and opposite. From this fact, one can deduce the concentration gradients in Fig. 6(b). The concentration of CO_2 at $x = x_f$ is

$$c^{*}_{CO_2} = \frac{D_{O_2}\, c^{L}_{O_2}}{D_{CO_2}} \tag{10}$$

Equation (7) for CO and CO_2 in Region II (Fig. 6(a)) is more complex, as now there is a convection term since the stoichiometry of reaction (3) requires

$$J^{II}_{CO} = -2 J^{II}_{CO_2} \tag{11}$$

Thus equation (7) for CO_2 becomes

$$J^{II}_{CO_2} = -D_{CO_2}\left(\frac{\partial c_{CO_2}}{\partial x}\right) - \frac{c_{CO_2}\, J^{II}_{CO_2}}{c_T} \tag{12}$$

Rearranging to separate variables gives

$$J^{II}_{CO_2}\, dx = -D_{CO_2}\left(\frac{c_T}{c_T + c_{CO_2}}\right) dc_{CO_2} \tag{13}$$

This can be integrated from $c_{CO_2} = c^{*}_{CO_2}$ at $x = x_f$ and $c_{CO_2} = c^{0}_{CO_2}$ at $x = 0$:

$$J^{II}_{CO_2} = \frac{-D_{CO_2}\, c_T}{x_f} \ln\left(\frac{c_T + c^{*}_{CO_2}}{c_T + c^{0}_{CO_2}}\right) \tag{14}$$

This can be simplified further using equation (10) and the fact that $c^{*}_{CO_2} \gg c^{0}_{CO_2}$:

$$J^{II}_{CO_2} = \frac{-D_{CO_2}\, c_T}{x_f} \ln\left(1 + \frac{D_{O_2}\, c^{L}_{O_2}}{D_{CO_2}\, c_T}\right) \tag{15}$$

A mass balance between CO and O_2 gives

$$J^{II}_{CO} = -2 J^{I}_{O_2} \tag{16}$$

Combining this with equation (11),

$$J^{II}_{CO_2} = J^{I}_{O_2} \tag{17}$$

When equation (15) is combined with equations (17) and (9a),

$$J_{CO_2}^{II} = \frac{-D_{O_2}c_{O_2}^L}{(L-x_f)} = \frac{-D_{CO_2}c_T}{x_f}\ln\left(1+\frac{D_{O_2}c_{O_2}^L}{D_{CO_2}c_T}\right) \tag{18}$$

Solving for L/x_f gives

$$\frac{L}{x_f} = 1 + \frac{D_{CO_2}c_{O_2}^L}{D_{O_2}c_T}\left[\ln\left(1+\frac{D_{O_2}c_{O_2}^L}{D_{CO_2}c_T}\right)\right]^{-1} \tag{19}$$

Next the gas phase diffusivities, D_{i,N_2}, of O_2 in N_2 and CO_2 in N_2 must be estimated. This is done with the Chapman-Enskog correlation [14], which yields diffusivity in cm^2/s when the variables in the expression below are expressed in the appropriate units:

$$D_{i,N_2} = 0.0018583\left(\frac{1}{M_i}+\frac{1}{M_{N_2}}\right)^{1/2}T^{3/2}\left(\frac{1}{P\sigma_{i,N_2}^2\Omega}\right) \tag{20}$$

Here M_i is the molecular weight (g/mol) of species i, T is the absolute temperature (K), P is the pressure (atm), σ_{i,N_2} is the average of the molecular diameter (Å) of species i and N_2, and Ω_{i,N_2} is the collision integral (unitless). The later two were determined from the tables of Svehla [15] and Sherwood et al. [16]. Table II lists some calculated diffusivities. The value of L/x_f is also shown in Table II and is constant with temperature.

For narrow cracks, the contribution of Knudsen diffusion must also be considered. The combined effects of ordinary diffusion and Knudsen diffusion have been discussed by other investigators [9-10, 12]. In the Knudsen diffusion regime, molecule-wall collisions dominate over molecule-molecule collisions. The effective diffusivity, D^{eff}, is a combination of the ordinary diffusivity, D^{ord}, and Knudsen diffusivity, D^K. The combined effects of ordinary and Knudsen diffusion can be written as [17, 18]

$$\frac{1}{D^{eff}} = \frac{1}{D^{ord}} + \frac{1}{D^k} \tag{21}$$

When the mean free path is greater than 10 crack widths, then Knudsen diffusion is the dominating flow mechanism [17]. For the 1 atm total pressure used in this study, the mean free path is ~3.3×10^{-7} m. The machined slots are much larger than this, and even the craze cracks (~1.28×10^{-5} m) are larger than the mean free path. Thus at the 1 atm (101 325 Pa) pressure used in this study, the average crack width indicates a very small Knudsen contribution; however, at lower pressures which are closer to actual reentry pressure, the Knudsen contribution must be considered.

Now with values for x_f/L and the gas phase diffusivities carbon consumption can be calculated. As noted, this is simply the molar flux of $CO_2(g)$ emerging from the crack, as given by equations (9b) and (9a):

$$J_{CO_2}^{I} = \frac{D_{CO_2}c_{CO_2}^*}{(L-x_f)} = \frac{D_{O_2}c_{O_2}^L}{L\left[1-\left(\frac{x_f}{L}\right)\right]} \tag{22}$$

The denominator is written in the above form, since x_f/L is now a known quantity. The goal is to estimate the radius of the cavity formed below a crack, as shown in Fig. 6.

The flux of $CO_2(g)$ (eq. (11)) can be converted to a mass loss of carbon as

$$\frac{dW_C}{dt} = \frac{M_C}{M_{CO_2}} J^I_{CO_2} wl = \frac{M_C D_{O_2} P_{O_2} wl}{M_{CO_2} RTL \left[1 - \left(\dfrac{x_f}{L}\right)\right]} \tag{23}$$

Here W_C is the weight loss of carbon, M_C is the molecular weight of carbon (12 gm/mol), M_{CO_2} is the molecular weight of carbon dioxide (44 gm/mol), R is the gas constant, w is the crack width, and l is the crack length. Note that the wl term would be omitted for weight loss per unit area.

The weight loss with time can be related to the volume change with time of the cavity at the base of the crack. Assume a rectangular crack with a half-cylinder cavity of radius r growing at its base. In practice the nonideality of the crack is accounted for with a "tortuosity factor" [14]. For this approximation a tortuosity factor of 1 is assumed.

The weight loss can be related to the radius of the growing half-cylinder cavity as

$$\frac{dW_C}{dt} = \rho \frac{dV}{dt} = \rho \left[\frac{d\left(\dfrac{\pi r^2 l}{2}\right)}{dt}\right] \tag{24}$$

Here r is the radius of the half cylinder and ρ is the density of carbon/carbon taken to be 1.362 g/cm^3 [19]. Equating equations (24) and (25) and separating variables gives

$$d\left(\frac{\pi r^2 l}{2}\right) = \frac{M_C D_{O_2} P_{O_2} wl \, dt}{M_{CO_2} \rho RTL \left[1 - \left(\dfrac{x_f}{L}\right)\right]} \tag{25}$$

Integrating and solving for r results in the following:

$$r = \sqrt{\frac{2 M_C D_{O_2} P_{O_2} wt}{M_{CO_2} \pi \rho RTL \left[1 - \left(\dfrac{x_f}{L}\right)\right]}} \tag{26}$$

Note the crack length cancels out and does not appear in the final expression. Equations (23) and (26) are the key equations used to calculate oxidation damage.

3.2 Diffusion through the Slot *and* Growing Oxidation Cavity

Figure 2(a) shows that oxidation through a machined slot has produced a sizable oxidation void. Clearly now the model must include transport in the oxidation void as well as the increasing area of reaction. This situation is shown schematically in Fig. 6(c). Note also the symmetry of the oxidation void—it is best described with polar coordinates. The steady state flux for CO_2 entering this cylindrical geometry is [20]:

$$\frac{d}{dr}\left(r J_{CO_2}\right) = 0 \tag{27}$$

Taking the integration constant to be β, we have:

$$J_{CO_2} = \frac{\beta}{r} \tag{28}$$

We shall simply consider the oxidation cavity as an extension of region II in the slot (Figure 2(a)). Thus we leave reaction (4) at the same location in the slot or crack in the SiC coating as in the case for diffusion in the slot or crack only. We take the area at the top of cavity which is connected to the crack as A'. It is now more convenient to use flux as a weight/(unit time) by multiplying flux in weight/(unit area-unit time) by A'. So in analogy with equation (12), we have the following equation for the CO_2 flux entering the oxidation trough, $J^{tr}_{CO_2}$:

$$J^{tr}_{CO_2} A' = -D_{CO_2} A' \left(\frac{\partial c_{CO_2}}{\partial r} \right) - \frac{A' c_{CO_2} J^{tr}_{CO_2}}{c_T} \tag{29}$$

Equation (28) allows separation of variables:

$$J^{tr}_{CO_2} A' \, dr = \frac{\beta}{r} A' \, dr = -D_{CO_2} A' \left(\frac{c_T}{c_T + c_{CO_2}} \right) dc_{CO_2} \tag{30}$$

Integrating from $r = r_1$ $c_{CO_2} = c^{r_1}_{CO_2}$ to $r = r_2$ $c_{CO_2} = c^{r_2}_{CO_2}$ gives:

$$\beta A' \ln \frac{r_2}{r_1} = -D_{CO_2} A' c_T \ln \left(\frac{c_T + c^{r_2}_{CO_2}}{c_T + c^{r_1}_{CO_2}} \right) \tag{31}$$

So the flux at $r = r_1$ is:

$$J^{tr}_{CO_2} A' = \frac{\beta A'}{r} = - \frac{D_{CO_2} A' c_T \ln \left(\frac{c_T + c^{r_2}_{CO_2}}{c_T + c^{r_1}_{CO_2}} \right)}{r_1 \ln \left(\frac{r_2}{r_1} \right)} = - \frac{D_{CO_2} \pi r_1 l c_T \ln \left(\frac{c_T + c^{r_2}_{CO_2}}{c_T + c^{r_1}_{CO_2}} \right)}{r_1 \ln \left(\frac{r_2}{r_1} \right)} \tag{32}$$

This is then equated to the expression derived in the previous section for the flux of CO_2 going into region II. We are equating an expression in Cartesian coordinates to an expression in polar coordinates and there is a small section from $x = 0$ to $r = r_1$ (see Figure 6(c)), which is ignored in this approximation. The two fluxes, expressions (18) and (32), are equated. Note that we have reversed the sign in equation (32) as the polar coordinate system in the oxidation void is in the opposite direction from the Cartesian coordinate system in the crack.

$$\frac{-D_{CO_2} c_T r_1 l}{x_f} \ln \left(\frac{c_T + c^{*}_{CO_2}}{c_T + c^{r_1}_{CO_2}} \right) = \frac{D_{CO_2} \pi l c_T \ln \left(\frac{c_T + c^{r_2}_{CO_2}}{c_T + c^{r_1}_{CO_2}} \right)}{\ln \left(\frac{r_2}{r_1} \right)} \tag{33}$$

This simplifies to:

$$\ln \left(\frac{c_T + c^{*}_{CO_2}}{c_T + c^{r_1}_{CO_2}} \right) \ln \left(\frac{r_2}{r_1} \right) = \frac{-\pi x_f}{r_1} \ln \left(\frac{c_T + c^{r_2}_{CO_2}}{c_T + c^{r_1}_{CO_2}} \right) \tag{34}$$

We need to solve for $c_{CO_2}^{r_1}$. In order to do this we need to invert and expand the ln function:

$$\ln x = (x-1) - \frac{1}{2}(x-1)^2 + \ldots \quad (2 \geq x > 0) \tag{35}$$

We use only the first term and obtain:

$$\left(\frac{c_{CO_2}^{r_1} - c_{CO_2}^{*}}{c_T + c_{CO_2}^{*}} \right) \ln\left(\frac{r_2}{r_1} \right) = \frac{-\pi x_f}{r_1} \left(\frac{c_{CO_2}^{r_1} - c_{CO_2}^{r_2}}{c_T + c_{CO_2}^{r_2}} \right) \tag{36}$$

Solving for $c_{CO_2}^{r_1}$ gives:

$$c_{CO_2}^{r_1} = \frac{\left(\dfrac{c_{CO_2}^{*}}{c_T + c_{CO_2}^{*}} \right) \ln\left(\dfrac{r_2}{r_1} \right) + \dfrac{\pi x_f}{r_1} \left(\dfrac{c_{CO_2}^{r_2}}{c_T + c_{CO_2}^{r_2}} \right)}{\left[\left(\dfrac{1}{c_T + c_{CO_2}^{*}} \right) \ln\left(\dfrac{r_2}{r_1} \right) + \left(\dfrac{\pi x_f}{r_1 \left(c_T + c_{CO_2}^{r_2} \right)} \right) \right]} \tag{37}$$

This expression has the correct limits in that:

$$r_2 \to r_1 \quad c_{CO_2}^{r_1} \to c_{CO_2}^{r_2} \tag{38a}$$

$$x_f \to 0 \quad c_{CO_2}^{r_1} \to c_{CO_2}^{*} \tag{38b}$$

Putting this expression for $c_{CO_2}^{r_1}$ into the expression for the flux of CO₂, noting that $c_{CO_2}^{r_2}$ is close to zero, and simplifying gives

$$J_{CO_2} A = \frac{D_{CO_2} \pi l c_{CO_2}^{*}}{\ln\left(\dfrac{r_2}{r_1} \right) + \left(c_T + c_{CO_2}^{*} \right)\left(\dfrac{\pi x_f}{r_1 c_T} \right)} \tag{39}$$

Next we need to determine the change of radius r_2 with time:

$$\frac{dV}{dt} = \frac{r_2 d(\pi r_2 l)}{dt} = \frac{M_C}{M_{CO_2}} \frac{1}{\rho} J_{CO_2}^{tr} A = \frac{M_C}{M_{CO_2}} \frac{1}{\rho} \left\{ \frac{D_{CO_2} \pi l c_{CO_2}^{*}}{\ln\left(\dfrac{r_2}{r_1} \right) + \left(c_T + c_{CO_2}^{*} \right)\left(\dfrac{\pi x_f}{r_1 c_T} \right)} \right\} \tag{40}$$

Simplifying and separating variables gives:

9

$$\left(r_2\ln(r_2)-r_2\ln(r_1)+r_2\left(c_T+c^*_{CO_2}\right)\left(\frac{\pi x_f}{r_1 c_T}\right)\right)dr_2 = \frac{M_C}{M_{CO_2}}\frac{D_{CO_2}c^*_{CO_2}}{\rho}dt \tag{41}$$

This can be integrated from $t=0$ at $r_2=r_1$ $t=t$ at $r_2=r_2$, leading the expression:

$$t = \frac{M_{CO_2}}{M_C}\frac{\rho}{D_{CO_2}c^*_{CO_2}}\left[\frac{r_2^2}{2}\ln(r_2)-\frac{r_2^2}{4}-\frac{r_2^2}{2}\ln r_1 +\frac{r_2^2}{2}\left(\frac{\pi x_f\left(c_T+c^*_{CO_2}\right)}{r_1 c_T}\right)+\frac{r_1^2}{4}-\frac{r_1^2}{2}\left(\frac{\pi x_f\left(c_T+c^*_{CO_2}\right)}{r_1 c_T}\right)\right] \tag{42}$$

We can convert this to weight change of the growing half cylinder and obtain the expression:

$$W = \frac{\pi\rho(r_2-r_1)^2 l}{2} \tag{43}$$

$$t = \frac{M_{CO_2}}{M_C}\frac{\rho}{D_{CO_2}c^*_{CO_2}}\left[\begin{array}{c}\dfrac{\left(\sqrt{\dfrac{2W}{\pi\rho l}}+r_1\right)^2}{2}\ln(\sqrt{\dfrac{2W}{\pi\rho l}}+r_1)-\dfrac{\left(\sqrt{\dfrac{2W}{\pi\rho l}}+r_1\right)^2}{4}-\dfrac{\left(\sqrt{\dfrac{2W}{\pi\rho l}}+r_1\right)^2}{2}\ln r_1 \\[4mm] +\dfrac{\left(\sqrt{\dfrac{2W}{\pi\rho l}}+r_1\right)^2}{2}\left(\dfrac{\pi x_f\left(c_T+c^*_{CO_2}\right)}{r_1 c_T}\right)+\dfrac{r_1^2}{4}-\dfrac{r_1^2}{2}\left(\dfrac{\pi x_f\left(c_T+c^*_{CO_2}\right)}{r_1 c_T}\right)\end{array}\right] \tag{44}$$

Equation (42) and (44) replace equations (26) and (24) as expressions for cavity growth when diffusion in *both* the slot or crack and the cavity are considered.

3.3 Variation of Crack Width due to Thermal Expansion and Contraction

An important consideration is the variation of the crack width with temperature. This is minor for the machined slots, but significant for the craze cracks. The actual coating is not dense SiC, but rather converted carbon-carbon fibers and carbon matrix material. For this approximation the accepted coefficient of thermal expansion (CTE) for SiC as ~6.1×10^{-6} K^{-1} is used [21]. The thermal expansion along a carbon fiber is taken as 1×10^{-6} K^{-1} [22]. This puts the coating in tension on cool down, which leads to the cracks during processing. However, it leads to compression and possible crack closing during heat-up to temperatures above the processing temperature. The extent of crack closure can be estimated as

$$w_{RT} = \Delta\alpha s(T_P-T) \tag{45}$$

Here w_{RT} is the crack width at room temperature, $\Delta\alpha$ is the difference between the CTE of SiC and that of the carbon/carbon, s is the crack spacing, T_P is the processing temperature (taken as ~1650 °C), and T is the operating temperature. Since the crack width at room temperature is 12.8±1.4 µm, the crack spacing is calculated to be 1.5±0.2 mm from the equation above, reasonably close to that measured given the approximation of the CTEs. This calculated crack spacing is used in the above equation to estimate crack width at the oxidation temperature. At 1200 °C the crack width was calculated to be 7.1 µm.

3.4 Effect of Crack Wall Oxidation

Oxidation along the SiC crack wall may affect the rate of carbon/carbon oxidation. As will be discussed, the samples gain considerable weight due to passive oxidation. Microscopy indicates that thin films of SiO_2 form on

both the internal and external surfaces of the SiC coating. Fig. 7 shows the mouth of a crack and only a thin (~0.25-μm) film of SiO$_2$.

On the basis of the thin films of oxide observed, the oxidation rate constants for high-purity chemically vapor deposited (CVD) SiC [23] are used. The results shown in Table III are somewhat lower than the thicknesses of the oxide film on both the slots and cracks. It is probable the lower purity SiC in the conversion coating has an oxidation rate constant of an order of magnitude or so greater than that of CVD SiC. Such behavior is well documented [24]. Nonetheless images such as those in Fig. 7 indicate that under the conditions of this study, crack closure due to wall oxidation can be neglected.

4. Results and Discussion: Measured Oxidation Kinetics and Comparison with Model

4.1 Oxidation Below Machined Slots in SiC Coating

Specimens were oxidized at 1200 °C and examined with both CT and optical microscopy. Cross-sectional micrographs for the cavity formed below a 0.37-mm slot is shown in Figs. 2(a). Oxidation damage below all slots exhibited this type of half-cylinder morphology. Figs. 8(a) and (b) show the x-ray CT information.

The data in Figs. 2(a) and 8 make several important points. The similarity between the CT images and the actual optical microscopy images give credibility to the use of CT imaging to precisely size and characterize the three-dimensional morphology of this type of oxidation damage [25]. Both the optical microscope images and the CT images indicated the oxidation damage occurs in the form of a half cylinder. On a macroscopic scale this indicates even attack in all directions, supporting diffusion control of the oxidation process and the use of a half cylinder in the model.

Using image analysis software the areas of the oxidation cavities were measured. Approximating these areas as semicircles allows calculation of effective radii. The experimental results are compared to the predictions from equations (26) and (42) in Figs. 9(a) and (b). Agreement with equation (42) is remarkably good, indicating this is the preferred approach to modeling such oxidation behavior.

A second set of experiments was done to follow the kinetics of oxidation below machined slots with weight loss as the indicator of oxidation damage. Kinetics were followed using interrupted weight loss measurements. A typical kinetic curve is shown in Fig. 10. Note there is an initial weight gain, which is likely passive oxidation of the SiC, followed by a weight loss. The passive oxidation of the SiC will be discussed in the following section. The rates of weight loss are the carbon oxidation rates per the exposed area of carbon, which was determined from the slot dimensions. Note that the experimental weight loss rates appear to be roughly linear. It was found that the linear terms in equation (44) tended to dominate and thus the results from equation (44) were plotted and fitted to a linear rate for comparison to experiment.

Table IV compares the measured rates with those predicted from equation (44). Rates are normalized per unit area of exposed carbon, and hence the predictions are all the same for the given temperature of 1200 °C. The error in the predicted oxidation rate values is due to uncertainty in the measurement of slot depth (coating thickness). The calculated rates are within a factor of 1 to 2.6x the measured, which is reasonable.

4.2 Oxidation Below Craze Cracks in the SiC Coating

Having established the validity of the model with the machined slots, it is now appropriate to proceed to the more realistic situation of craze cracks in the SiC coating. Now there is a less well-defined geometry, as illustrated with the crack pattern in Fig. 4 and crack width measurement in Fig. 5. Nonetheless these measurements can be used to estimate approximate values for the diffusion model.

Oxidation kinetics for these specimens were followed with a recording thermobalance that enabled continuous weight change measurements. Results for 1000, 1100, 1200, and 1300 °C are given in Figs. 11(a) to (d). These data are reported in weight change per geometrical surface area. As will be discussed, the geometric surface area must be modified for actual reactive area of oxidation, which is different for each of the two processes occurring.

The oxidation kinetics suggest a combined parabolic/linear rate law. The initial weight gain observed at the three higher temperatures is likely due to the passive oxidation of SiC, which is parabolic:

$$\left(\frac{\Delta M}{A}\right) = \sqrt{k_p t} \tag{46}$$

Here $\left(\dfrac{\Delta M}{A}\right)$ is the specific weight change (weight per unit area), k_p is the parabolic rate constant, and t is the time.

The specific weight change over the surface area A of the SiC is taken as the geometric area of the sample disk. The weight loss after ~0.5 hr is linear with time and most likely due to carbon oxidation through the craze cracks. It is described by

$$\left(\frac{\Delta M}{A'}\right) = k_l t \tag{47}$$

Here k_l is the linear rate constant. Note that A' is the exposed area of carbon/carbon. This is the crack width at temperature multiplied by the total crack length for a particular sample.

The changes in the kinetic curves with temperature support the interpretation of the process as passive SiC oxidation coupled with C/C oxidation. At 1000 °C the initial parabolic regime was not observed; however, at 1200 and 1300 °C it was quite evident. This is due to the fact that passive oxidation of SiC shows a strong dependence on temperature [23]. Note, however, that the linear rate constant is relatively temperature independent. Diffusion-controlled oxidation of carbon shows only a weak temperature dependence, a combination of the $T^{1/2}$ dependence of the diffusion coefficient and the T^1 dependence of the crack closure due to thermal expansion. This dependence may not be evident in the limited data set in this study.

The combined passive oxidation of SiC/linear oxidation of carbon rate law is written as

$$\left(\frac{\Delta M}{A}\right)_{total} = \sqrt{k_p t} + k_l t \tag{48}$$

Here $\left(\dfrac{\Delta M}{A}\right)_{total}$ is the measured weight change per unit of geometrical area, k_p is the parabolic rate constant, t is the time, and k_l is the linear rate constant. This expression is similar to that used to describe the combined oxidation/vaporization of chromium alloys [26] and SiC [27], but this is somewhat simpler in that there are two independent processes occurring.

The dashed lines in Figs. 11(a) to (d) are fits of equation (48) to each kinetic curve. From these fits the parabolic and linear rate constants can be derived. Fits to the linear region are good; fits to the parabolic region are only approximate because of such factors as changing surface areas of passive oxidation and passive oxidation internal to the coating, which are not included in equation (48). The parabolic and linear rate constants extracted from the fit to the kinetic data are given in Table V. The parabolic rate constant was taken directly from the fit. Note that the listed parabolic rate constants are many orders of magnitude greater than those measured for high-purity SiC [23]. This is due to extensive internal oxidation of the porous SiC conversion coating. Measurements of the SiC conversion coating density have been reported to be 2.114 g/cm^3 [19]. When compared with the theoretical density of 3.217 g/cm^3 for SiC, this indicates a high amount of porosity. This porosity leads to the large extent of internal oxidation.

The linear rate constant shown in Table V was taken from the fit and multiplied by the geometrical surface area. This gives a rate of carbon oxidation per area of exposed carbon/carbon and allows direct comparison to the calculated rate in Table V. The predicted rates were obtained from equation (24).

The cracks in the SiC form a complex geometry. The oxidation cavities are an irregular shape as seen in the micrograph in Fig. 2(b). Fig. 12(a) shows the location of two CT scans, and Fig. 12(b) shows the results of the CT scans illustrating the varying size and shape of the oxidation cavity below a craze crack. The actual oxidation cavities are darker and are outlined in white in Fig. 12(b).

Despite this complex geometry of both the craze crack and the resultant oxidation damage, average values of crack width and length can be put into the oxidation model to estimate the rates. These are shown in Table V. The predicted and measured rates show very good agreement at 1000 and 1100 °C, which is remarkable given the irregular geometry of the cracks and corresponding oxidation damage as well as the approximations used in this study. We believe the larger variation at 1200 and 1300 °C may be due to volatile species in the conversion coating which the net weight loss measurement would necessarily include [4]. Observation of the both the 1000 and 1300 °C specimens after 2.5 hr indicate that the oxidation voids below the cracks are no longer distinct but start to merge, indicating that the approximation of the oxidation process as a single trough is no longer valid. This may be another reason for the discrepancy between the calculated and measured rates.

5. Conclusions

The kinetics of subsurface oxidation of SiC-protected reinforced carbon/carbon has been studied in the diffusion control regime (1000 to 1300 °C) in air. Specimens with machined slots in the SiC coating as well as specimens with natural occurring craze cracks in the SiC coating were tested. The geometry of these oxidation pathways was characterized with the aim of obtaining the exposed area of the carbon/carbon. For the craze cracks, crack closure due to shrinkage was considered. Oxidation of the SiC walls was shown to be negligible under the conditions of this study. Oxidation damage of the carbon/carbon was assessed with weight changes, CT scans, and optical microscopy of sections. The CT scans confirm the idealized half-cylinder shape of the oxidation cavity in the case of a slot. A two-step diffusion control model for carbon oxidation is adapted to describe the growth kinetics of this half cylinder. Two models were used—a simplified model which considered diffusion only in the slot or craze crack and a more detailed model which considered diffusion in both the slot or craze crack and the growing oxidation cavity.

Oxidation rates were first measured from optical microscopy of the growing oxidation cavity for the well-defined geometry of the slotted specimens. For these optical measurements, the data showed remarkably good agreement with the more detailed model which considered diffusion in the slot and the oxidation cavity. A series of experiments were also done where oxidation rates were followed with overall weight loss for both the specimens with slots and natural crazed cracks. For the weight loss measurements agreement to the model which considered diffusion in both the slot or craze crack and the growing oxidation cavity was reasonable.

Acknowledgments

References

1. D.M.Curry, J.W. Latchem, and G.B. Wisenhunt, in 21st AIAA Aerospace Sciences Meeting (AIAA, Reno, NV, 1983).
2. S.W. Yurgartis, M.D. Bush, and B.E. Mast, Surf. Coat. Tech. 70 (1994) 131.
3. F.J. Buchanan and J.A. Little, Surf. Coat. Tech. 53 (1992) 137.
4. N.S. Jacobson and D.M. Curry, Carbon 44 (2006) 1142.
5. W.H. Glime and J.D. Cawley, Carbon 33 (1995) 1053.
6. J.E. Medford, in 10th AIAA Thermophysics Conference (AIAA, Denver, CO, 1975).
7. J. Bernstein and T.B. Koger, J. Electrochem. Soc. 135 (1988) 2086.
8. E.L. Courtright, J.T. Prater, G.R. Holcomb, G.R. St. Pierre, and R.A. Rapp, Oxid. Met. 36 (1991) 423.
9. L. Filipuzzi, G. Camus, R. Naslain, and J. Thebault, J. Am. Ceram. Soc. 77 (1994) 459.
10. L. Filipuzzi and R. Naslain, J. Am. Ceram. Soc. 77 (1994) 467.
11. G.R. Holcomb, Corrosion 52 (1996) 531.
12. A. J. Eckel, J. D. Cawley, and T. A. Parthasarathy, J. Am. Ceram. Soc. 78 (1995) 972.
13. N.S. Jacobson, T.A. Leonhardt, D.M. Curry, and R.A. Rapp, Carbon 37 (1999) 411.
14. G.H. Geiger and D.R. Poirier, in "Transport Phenomena in Metallurgy," (Addison-Wesley, Reading, MA, 1973) p. 464.
15. R.A. Svehla, NASA TR−R-132 (1962).
16. T.K. Sherwood, R.L. Pigford, and C.R. Wilke, "Mass Transfer," (McGraw-Hill, New York, NY, 1975) p. 20.
17. C.J. Geankoplis, "Mass Transport Phenomena" (Ohio State University Bookstores, Columbus, OH, 1984), p. 152.
18. G.W. Hewitt, in "Chemistry and Physics of Carbon" (Marcel Dekker, New York, NY, 1965) p. 73.
19. S.D. Williams, D.M. Curry, D.C. Chao, and V.T. Pham, J. Thermophys. Heat Transfer, 9 (1995) 478.
20. R. Ghez, in "A Primer of Diffusion Problems" (Wiley, New York, NY, 1988) p. 43.
21. Y.S. Touloukian, R.K. Kirby, R.E. Taylor, and T.Y.R. Lee, in "Thermal Expansion Nonmetallic Solids" (IFI/Plenum, New York, NY, 1977) p. 873.
22. T. Ullmann, M. Shmücker, H. Hald, R. Henne, and H. Schneider, in Proceedings of 8th International Symposium on Materials in a Space Environment (Archachon, Frankreich, June 2000).
23. L. Ogbuji and E.J. Opila, J. Electrochem. Soc. 142 (1995) 925.
24. N.S. Jacobson, J. Am. Ceram. 76 (1993) 3.
25. D.J. Roth, N.S. Jacobson, J.N Gray, L.M. Cosgriff, J.R. Bodis, R.A. Wincheski, R.W. Rauser, E.A. Burns, and M.S. McQuarter, Ceram. Eng. Sci. Proc. 26 (2006) 133.
26. C.S. Tedmon Jr., J. Electrochem. Soc. 113 (1966) 766.
27. E.J. Opila and N.S. Jacobson, Oxid. Met. 44 (1995) 527.

Appendix—Symbols

A	area of SiC for oxidation
A'	area of exposed carbon-carbon for oxidation
c	molar concentration
D	diffusivity
J	molar flux
k	rate constant (weight^2/(unit area)^2-time)
L	depth of crack or coating thickness
l	crack length
M	molecular weight (g/mol)
P	total pressure in atmospheres
q	pore radius
R	gas constant
r	radius of half-cylinder cavity
s	crack spacing
T	temperature
t	time
v	molar velocity
W	weight loss
w	crack width
x	depth of crack coordinate with origin at SiC/C-C interface
x_f	depth to CO/CO_2 (region II) and CO_2/O_2 (region I) boundary
σ	average collision diameter between species i and N_2 (angstroms)
Ω	collision integral
α	coefficient of thermal expansion
β	integration constant for steady flux in cylindrical symmetry

Subscripts:

f	indicates boundary of regions I and II
i	species
l	linear
P	processing
p	parabolic
T	total
1	designates radius of half cylinder cavity before oxidation (taken as 0.5*crack width)
2	designates radius of half cylinder cavity after oxidation

Superscripts:

ave	average
eff	effective
K	Knudsen
L	indicates position L
ord	ordinary
0	indicates position 0
I	region I
II	region II
$*$	indicates position x_f

Figure Captions

Fig. 1.—Schematic of reinforced carbon/carbon (RCC).

Fig. 2.—Optical micrographs showing oxidation void in RCC formed below crack in SiC coating for (a) 0.37-mm slot in air at 1200 °C for 2.5 hr (b) 1100 °C and 0.0066 atm (667 Pa) for 1 hr.

Fig. 3.—Machined slots in RCC buttons.

Fig. 4.—Crack pattern on RCC disk. (a) Optical micrograph. (b) "Skeleton" trace of cracks.

Fig. 5.—Crack in SiC conversion coating.

Fig. 6.—Two-step diffusion control model. (a) Schematic of fluxes and boundaries for a slot or crack. (b) Relative concentrations of gases. (c) Schematic of idealized void.

Fig. 7.—Oxide film on surface of SiC coating (0.5 hr in air at 1200 °C) at crack opening. (a) Electron micrograph. (b) Oxygen map.

Fig. 8.—Computed tomography (CT) of machine-slotted SiC-coated RCC oxidized for 0.5 hr in air at 1200 °C. (a) CT sample locations. (b) Three CT slices. Slot near notch on left is 0.76 mm, and slot on right is 1.03 mm. (c) Three-dimensional reconstruction of disk.

Fig. 9.—Oxide cavity growth. (a) 0.53 mm slot. (b) 1.05 mm slot. Both plots show the calculated results from considering diffusion only in the slot and diffusion on the slot and growing cavity.

Fig. 10.—Weight loss oxidation kinetics determined from interrupted measurements for RCC specimen with 0.484-mm slot width at 1200 °C in air.

Fig. 11.— Weight loss oxidation kinetics for RCC in air. (a) 1000 °C. (b) 1100 °C. (c) 1200 °C. (d) 1300 °C.

Fig. 12.—Computed tomography (CT) of craze crack of SiC-coated RCC oxidized for 2.5 hr in air at 1143 °C. (a) Location of CT slices. (b) Two CT slices.

TABLE I. Measured crack parameters for SiC-coated carbon/carbon materials

SiC-coated carbon/carbon material	Coating thickness, mm	Crack length per unit area, mm^{-1}	Crack spacing, mm	Crack width, μm	Crack area per unit area
Present study, RCC	0.78±0.14	0.33±0.04	3.4±0.9	12.8±1.41	4.2×10^{-3}
Yurgartis et al. [2], Specimen A	0.3024±0.03866	2.985	0.6247±0.2233[a]	1.72±1.41	5.1×10^{-3}
Yurgartis et al. [2], Specimen B	0.2788±0.02853	3.555	0.6517±0.3356[a]	2.02±1.47	7.3×10^{-3}
Buchanan and Little [3]	----	----	----	----	(3–8)×10^{-4}

[a]Through coating thickness.

TABLE II. Diffusivities of $O_2(g)$ and $CO_2(g)$ in $N_2(g)$ and position of boundary between regions I and II (Fig. 6(a)). [Total pressure is 1 atm (101 325 Pa).]

Temperature, °C	D_{O_2, N_2}, cm^2/s	D_{CO_2, N_2}, cm^2/s	L/x_f
1000	2.38	1.86	2.13
1100	2.70	2.11	2.13
1200	3.03	2.38	2.13
1300	3.38	2.65	2.13

TABLE III. Estimated oxide film thicknesses on slot or crack walls of SiC coating

Temperature, °C	Rate constant		Oxide thickness	
	1 atm O_2,[a] μm^2/hr	0.21 atm O_2, μm^2/hr	0.5 hr in 0.21 atm O_2, μm	2.5 hr in 0.21 atm O_2, μm
1200	1.82×10^{-2}	3.78×10^{-3}	4.35×10^{-2}	9.72×10^{-2}
1300	3.76×10^{-2}	7.90×10^{-3}	6.28×10^{-2}	0.14

[a]From reference 23.

TABLE IV. Oxidation rates for SiC-coated
RCC specimens with machined slots
[At $T = 1200$ °C in air.]

Slot width, w, mm	Slot length, l, mm	Weight loss rate, mg/mm^2-hr	
		Measured	Calculated[a]
0.484±0.062	8.177±0.923	34±6	18.3
0.312±0.033	8.284±0.63	48±6	20.4
0.560±0.013	7.094±0.132	48±1	17.6
0.466±0.04	7.114±0.019	57±5	18.6
1.116±0.024	7.602±0.101	18±1	13.9
0.963±0.0041	7.624±0.039	21±1	14.7

[a]From equation (44).

TABLE V. Measured and calculated rates of RCC oxidation through craze cracks

Sample temperature, °C	Geometrical surface area, mm²	Total crack length,[a] mm	Crack width, μm	Area of carbon exposed by craze cracks,[b] mm²	Calculated linear rate,[c] mg/mm²·hr	Measured linear rate,[d] mg/mm²·hr	Measured parabolic rate,[e] mg²/mm⁴·hr
Room temperature			12.8±1.4				
1000	850.2±10	281±34	10.2±2.7	2.87±0.8	25	31±9	-----
1100	935.5±10	309±37	8.7±2.3	2.67±0.8	23.3	31±9	3.94×10^{-3}
1200	946.8±10	312±37	7.1±1.8	2.21±0.6	21.8	53±15	2.79×10^{-2}
1300	940.2±10	310±37	5.5±1.4	1.71±0.5	20.5	67±20	3.25×10^{-2}

[a]Equal to (geometrical area × crack length)/unit area.
[b]Equal to (total crack length) × (crack width).
[c]From equation (44).
[d]Area is exposed area of carbon/carbon.
[e]Area is geometrical surface area.